Solvent Annealing of PbI_2 for High-Quality Crystallization of Perovskite Films for Solar Cells with Efficiency Exceeding 18%

Yafei Wang[a], Shibin Li[a*], Peng Zhang[a], Detao Liu[a], Xiangling Gu[a], Hojjatollah Sarvari[b], Zhongbiao Ye[a,b], Jiang Wu[c], Zhiming Wang[d], and Zhi David Chen[a,b*]

[a] State Key Laboratory of Electronic Thin Films and Integrated Devices, and School of Optoelectronic Information, University of Electronic Science and Technology of China (UESTC), Chengdu, Sichuan 610054, China

[b] Department of Electrical & Computer Engineering, and Center for Nanoscale Science & Engineering, University of Kentucky, Lexington, Kentucky 40506, USA

[c] Department of Electronic and Electrical Engineering, University College London, Torrington Place, London WC1E 7JE, United Kingdom

[d] Institute of Fundamental and Frontier Sciences, University of Electronic Science and Technology of China, Chengdu, 610054, China

*Corresponding authors: shibinli@uestc.edu.cn, zhichen@engr.uky.edu

Abstract

Most works focused on solvent annealing of perovskite. In this work, we focused on solvent annealing of lead iodide. Based on the two-step spin coating method, we designed a screening method to search for an effective solvent annealing process for PbI_2. PbI_2 films were annealed in diverse solvent atmospheres including DMF, DMSO, Acetone and Isopropanol (IPA). We found that solvent annealing of PbI_2 in the DMF, Acetone, and IPA atmospheres resulted in dense PbI_2 films, which impedes complete conversion of PbI_2 to $CH_3NH_3PbI_3$. Surprisingly, employing the DMSO solvent annealing process for PbI_2 led to porous PbI_2, which helped complete conversion of PbI_2 to perovskite with larger grain sizes. Solar cells fabricated using the DMSO solvent annealing process exhibit the best efficiency of 18.5% with a fill factor of

76.5%. This unique solvent annealing method presents a new way for controlling the perovskite film quality for highly efficient solar cells.

1. Introduction

Organic/inorganic trihalide lead-based perovskite solar cells have attracted much attention because of their superb photovoltaic performance and low-cost solution processes. Since the first report of perovskite solar cells in 2009, the power conversion efficiency (PCE) has increased from 3.8% to today's 21%.[1-2] In order to achieve more efficient photoelectric conversion, device structures, recombination mechanisms, interface engineering and materials synthesis need to be studied.

For fabrication of low-cost and high-quality perovskite solar cells, solution-based processes are widely used. There are two main solution-based synthesis methods for fabrication of perovskite thin films: one-step solution process and two-step sequential deposition method. The first solid-state perovskite solar cell was reported by Park group in 2012, which actually triggered perovskite solar cell research activities.[3] In 2013, a two-step sequential deposition method was proposed to produce high-quality perovskite films. [4] In order to control the morphology better, Park et al.[5] investigated the influence of MAI concentrations on morphology of perovskite grains. Moreover, they modified the above sequential deposition method through replacing dipping with spin-coating in the second step. Then cuboid $CH_3NH_3PbI_3$ crystals with controllable sizes were achieved. Park group also fabricated $FAPbI_3$ solar cells via two-step spin-coating method in 2014.[26] Generally, the two-step sequential deposition method can be used easily to achieve controllable morphology

of perovskite films. However, in the two-step method, it is difficult for PbX_2 to be completely transformed into perovskite.[6] Although there is not a consistent conclusion on the effect of residual lead iodide on the defects, the residual lead iodide does negatively affect the efficiency, which is more serious in the two-step deposition method.

Meanwhile, solvent engineering and solvent annealing have been used to improve the morphology of films and to decrease residual lead iodide. Seok et al reported a mixed solvent engineering process for fabrication of efficient perovskite solar cells with a certified power-conversion efficiency of 16.2%.[14] In this procedure, a mixed solvent of GBL and DMSO was used in a one-step spin-coating process followed by toluene drop-casting, leading to uniform and dense perovskite layers. Park et al. also fabricated highly reproducible perovskite solar cells via a mixed solvent (DMSO/DMF) engineering used in the one-step deposition method. Diethyl ether was used to remove DMF solvent in this process. Average power conversion efficiency (PCE) of 18. 3% and the best efficiency of 19. 7% were attained. [15] Solvent annealing was introduced for perovskite fabrication in 2014 by Huang et al. [8] In their investigation, DMF as an annealing solvent for perovskite did increase the $CH_3NH_3PbI_3$ grain sizes and crystallinity. In order to obtain better quality perovskite films, different solvents and methods were adopted in solvent annealing.[9-13, 27, 28] These investigations improved grain growth, crystallization, and morphology. Compared to the mixed-solvent process, solvent annealing is more suitable for surface morphology modification. The vapors eliminate grain boundaries so that the film morphology is improved. Therefore, solvent vapor annealing effectively improves crystallinity and morphology of perovskite films.

Regarding solvent annealing processes, most works were focused on annealing

perovskite films in solvent atmospheres. In this work, we focused on studies of annealing PbI_2 films instead of annealing perovskite. We designed a screening method to search for an effective solvent annealing process, which led us to discover a new solvent annealing process. PbI_2 annealing in the DMSO solvent in the first step led to a best solar cell with a PCE of 18. 5% and a fill factor of 76. 5%. During screening we studied different annealing ambiances of lead iodide films on crystallinity and morphology of both PbI_2 and perovskite layers.

2. Results and Discussion

In previous reports, solvent annealing was carried out on perovskite, which is important for controlling the quality of perovskite films. [19] We studied solvent annealing of PbI_2 instead of perovskite. As shown in Figure 1(a), we designed a screening method for identifying the most efficient solvent annealing process for PbI_2. The PbI_2 films were fabricated using a two-step heating process, in which in the first step PbI_2 films were heated at 45°C for 5 min and then in the second step heated to 100°C for 5 min. As shown in Figure 1(a), there are four annealing processes: (1) first step thermal annealing and second step thermal annealing (TA-TA); (2) first step thermal annealing and second step solvent annealing(TA-SA); (3) First step solvent annealing and second step solvent annealing (SA-SA); (4) first step solvent annealing and second step thermal annealing (SA-TA). Thermal annealing (TA) was carried in nitrogen. We considered four solvents: DMF, DMSO, Acetone, and IPA and three processes in which solvents were involved. On considering three processes and four solvents, we have 12 experimental cases.

We first used DMF as the annealing solvent. The absorption spectra of PbI_2 and perovskite prepared using these four annealing processes were measured as shown in Fig. 1(b)

and (c). Fig. 1(b) shows that three absorptions (0.703, 0.713, 0.737) at ~550 nm of PbI_2 films obtained using the SA-TA, SA-SA, and TA-SA processes are slightly larger than that (0.682) of the PbI_2 films prepared using the TA-TA processes. This suggests that first step annealing in DMF at 45°C improves the optical absorption at a wavelength of ~550 nm. Based the above annealed PbI_2 films, perovskite films were obtained by reaction with MAI as described in the Experimental section. Fig. 1(c) shows that absorptions (0.361, 0.363) of $CH_3NH_3PbI_3$ perovskite films prepared from PbI_2 films using the DMF SA-TA and DMF SA-SA processes are larger than that (0.254) of the perovskite films prepared from PbI_2 films using the TA-TA and DMF TA-SA processes. Thus, there are two better processes, DMF SA-TA and DMF SA-SA. The DMF SA-SA process resulted in the largest absorption of perovskite, but its baseline is higher than other three processes'. This is caused by stronger light scattering due to the rough surface of perovskite. [19] The rough surface of perovskite was induced by the PbI_2 films obtained by using the DMF SA-SA process, which might be due to the higher temperature annealing in DMF in the second step. It is known that rough surface of perovskite is not good for solar cells. Therefore, the DMF SA-SA process cannot be used and we select DMF SA-TA process. Figure 1(d) presents a supporting evidence. The XRD main peak (001) of the PbI_2 film prepared in the DMF SA-TA process is much larger than that prepared in the TA-TA processes. As shown in Figure 1(e), the forward and reverse scan J-V curves exhibit different I-V hysteresis behaviors of perovskite solar cells for each annealing method using DMF solvent. With the lower temperature (45°C) solvent annealing (SA-SA, SA-TA), the perovskite solar cells show smaller hysteresis than the devices fabricated with TA-TA or TA-SA processes. The reduction of hysteresis is owing to the better crystallization

of lead iodide and perovskite. The improved morphology of perovskite films also contributes to the suppression of hysteresis. [29]

In principle, right after spin-coating, the PbI_2 films are wet with DMF. There still are many PbI_2 molecules or clusters in the DMF solution. The lower temperature annealing may result in precipitation of PbI_2 due to slow evaporation of DMF so that crystal grains increase slowly. In the two-step annealing, the preliminary crystal grains are formed at the lower temperature annealing in the first step, and in the second step the remaining DMF solvent is removed quickly at the higher temperature annealing because the evaporation rate of DMF at 100°C is much larger. [21] It is clear that the lower temperature annealing in the first step determines the major crystallization of PbI_2 while the higher temperature annealing in the second step may just slightly modify the PbI_2 crystal grains. Therefore, we believe that solvent annealing in other ambiences at a lower temperature in the first step might affect the crystallization and morphology of PbI_2 more effectively than that at a higher temperature in the second step. Therefore, we chose the SA-TA process for all other ambiences (DMSO, Acetone, and IPA), which is marked as a star in Figure 1(a).

Using the SA-TA process for PbI_2, we studied effects of four different solvent ambiences (DMF, DMSO, Acetone and IPA) on the surface morphology of PbI_2 and perovskite films as shown in Figure 2. Among all the processes, the DMF SA-TA process resulted in the largest crystals of PbI_2, but with a very rough surface. We also observed that the film was very dense. The surface morphologies of PbI_2 films prepared in TA-TA, Acetone SA-TA, and IPA SA-TA are similar, which are smoother with smaller crystal grains than in DMF and DMSO SA-TA processes. It is of particular interesting to see that PbI_2 films prepared in DMSO SA-TA are

porous. After conversion of PbI_2 to perovskite, surface morphologies of perovskite films are shown in Figures 2(f)-(j). There are two groups. TA-TA, DMF SA-TA, DMSO SA-TA resulted in larger cuboid crystal grains of perovskite films, and the DMSO SA-TA process resulted in the largest crystal grains. Acetone SA-TA and IPA SA-TA produced smaller crystal grains with smoother morphologies of perovskite films.

As shown in Figure 3(a), XRD studies showed that the main peak (001) of the PbI_2 film prepared in DMF SA-TA is the largest, that prepared in Acetone SA-TA, IPA SA-TA, and TA-TA processes are lower, and that prepared in DMSO SA-TA is the lowest. These are consistent with the SEM images in Figure 2(a)-(e). This suggests that the DMSO SA-TA process results in nearly complete conversion of PbI_2 to perovskite. UV-vis absorption studies showed that absorptions of PbI_2 films prepared in all solvent annealing processes are slightly larger than the absorption of the PbI_2 film prepared in the TA-TA process (See Figure 3(b)). In Figure 3(c) we took photos of PbI_2 and perovskite films processed in various processes and found that the surfaces of the DMF SA-TA and DMSO SA-TA processed samples look like fog or clouds, suggesting stronger light scattering. This observation is also consistent with the higher baselines of the UV-vis absorptions for the DMF SA-TA and DMSO SA-TA processed samples in Figure 3(b).

After conversion of PbI_2 to perovskite, the XRD studies in Figure 3(d) showed that the main peak (110) of the perovskite film prepared in DMSO SA-TA is the largest, the main peaks (110) of the perovskite films prepared in TA-TA, DMF SA-TA, and IPA SA-TA are lower, and the main peak (110) of the perovskite film prepared in Acetone SA-TA is the lowest. Regarding the crystal grain sizes, the DMSO SA-TA process is the best. In addition to

crystal quality, another important issue is the remaining PbI_2 after conversion to perovskite. As shown in Figure 3(d), the main peak (001) at 12.4° of PbI_2 indicates the remaining PbI_2. The peak (001) of PbI_2 for the sample prepared in DMSO SA-TA is much lower than those prepared in TA-TA, DMF SA-TA, Acetone SA-TA, and IPA SA-TA processes. The UV-vis studies of perovskite in Figure 3(e) showed that the absorptions (0.327) at ~770nm of the perovskite films prepared in DMSO SA-TA and DMF SA-TA are much larger than those (0.268) of the perovskite films prepared in TA-TA, Acetone SA-TA, and IPA SA-TA processes. It is interesting to notice that at wave lengths of <500nm the absorption of the DMSO SA-TA processed sample is much lower than other samples. We believe that the remaining PbI_2 helped absorptions in other samples. Because of little remaining PbI_2 in the DMSO SA-TA processed sample the absorption at wave lengths of <500nm should be much less. This is consistent with the XRD results in Figure 3(d). The current (J)-voltage (V) curves of samples processed in different solvent annealing ambiences are shown in Figure 3(f). It can be seen that the DMSO SA-TA processed sample exhibits the best power conversion efficiency (PCE), which is 17.1%. Table I shows parameters (PCE, FF, V_{oc} and J_{sc}) of devices fabricated using TA-TA, DMF SA-TA, DMSO SA-TA, Acetone SA-TA and IPA SA-TA processes. It can be seen clearly that the FF of DMSO SA-TA processed sample reaches 78.1 which is much better than that of other annealing processed samples. The V_{oc} and J_{sc} of the device treated by DMSO SA-TA process are 1.04 V and 20.68 mA/cm^2 which are quite high compared with other devices.

It is very interesting to understand why the DMSO SA-TA process can produce solar cells with the highest PCE. A schematic solvent vapor annealing mechanism is shown in

Figure 4. In TA-TA, DMF SA-TA, Acetone SA-TA, and IPA SA-TA, PbI_2 cannot be completely converted to perovskite because PbI_2 films are dense, preventing the MAI solution from diffusion through the PbI_2 films. Only the DMSO SA-TA process resulted in porous PbI_2 film as shown in the SEM image in Figure 2(c). We noticed that Yi et al. [6] reported solar cells based on bilayer porous PbI_2 films obtained using PbI_2 solutions of mixed DMF/DMSO without solvent annealing. We did not see their paper until we finished most of our experiments. Our method is obviously different from theirs because we used DMSO solvent annealing. The porosity on the surface of our PbI_2 samples is more than that of their samples. Because of its porosity, the MAI solution can easily diffuse through the PbI_2 film and reacts with PbI_2 more completely. During DMSO vapor annealing, DMSO molecules break the crystal lattice of PbI_2 films because of their strong binding ability with Pb^{2+}. [8] In the first step low temperature annealing of the PbI_2 film in DMSO, DMSO molecules attach to the DMF solvent and are bond to Pb^{2+} ion tightly. The DMSO-PbI_2 complexes exist until the beginning of high temperature (100°C) annealing in the second step. When the DMSO is released during this heating step, pores are gradually formed in the PbI_2 film. Thus, MAI can penetrate into the PbI_2 layer deeply through the porous structure. At the same time, these pores provide enough space for the perovskite grain growth. The grains increase freely in every directions. Finally, the dense perovskite film with large grain sizes and without residual PbI_2 is obtained. Cross-sectional SEM analysis shows that the grain sizes of the perovskite based on the DMSO SA-TA process are larger and more like cuboid crystals as shown in Figure 4(b) and (c), which may greatly enhance charge extraction. The larger grains as the capping layer may perfectly connect the HTM directly with the perovskite coated on m-TiO_2,

resulting in less boundaries in the transport path of carriers. On the contrary, perovskite films based on the TA-TA annealing process exhibit smaller grains and more grain boundaries as shown in Figure 4(b).

To probe the charge transport properties of the solar cells, we performed the electrochemical impedance spectroscopy (EIS) in Figure 4(d). Two semicircles were obtained in the Nyquist plots. By fitting with a simple equivalent circuit model we investigated the charge transport process in the photovoltaic devices. Based on the previous reports, R_1 represents the contact resistance which is obtained from the intercept in the x-axis of the high frequency curve. [11, 22, 23] We observed that the values of R_1 for these two devices were almost identical in the vicinity of 60 ohms, indicating that the DMSO SA-TA process has little effect on the contact resistance. The first semicircle in the high frequency range was mainly attributed to the transfer resistance (R_2). The device fabricated from the DMSO SA-TA process exhibits a lower value of R_2 probably due to a better film coverage and charge-transfer ability. This result is consistent with the above discussion about the larger grain size and less lead iodide residue increasing the carrier transport performance. The second arc is related to the recombination resistance (R_3). Obviously, the curve of this recombination resistance for the sample treated by the DMSO SA-TA process shows a larger value than that for the sample treated by the TA-TA process. A larger recombination resistance indicates a lower recombination loss that is also attributed to bigger grains and less boundaries. Generally, carriers could be more easily collected when the charges needn't go through too many boundaries which always act as carriers trapping centers. This analysis clearly suggests that the DMSO SA-TA process based solar cells should exhibit excellent

efficiency.

We carried out extensive experiments with different m-TiO_2 particle diameter, volume of annealing solvent, and the spin-coating speed to explore the optimum experiment parameters. The results are included in the supporting information.

After optimization, we fabricated the devices with their structure as follow: fluorine doped tin oxide (FTO)/compact TiO_2/mesoporous TiO_2/$CH_3NH_3PbI_3$/spiro-OMeTAD (HTM)/Au contact. Under 1 illumination intensity of 100 mW cm^{-2}, the best performance device based on DMSO solvent annealing exhibits a short-circuit current density (J_{SC}) of 22. 86 mA cm^{-2}, an open-circuit voltage (V_{OC}) of 1057 mV, and a FF of 0.765, resulting in a PCE of 18.5% of reverse scan (See Figure 5(a)). We observed that the hysteresis between the reverse and forward scan is negligible too. The effective improvement of the crystallinity and grain size of perovskite films is the reason for the enhancement of photoelectric performance. The external quantum efficiency (EQE) spectra was measured as shown in Figure 5(b). The perovskite with DMSO solvent annealing shows a wide photo response from 360 nm to 760 nm, which reaches the highest value of 94%. The estimated J_{SC} value was about 22 mA cm^{-2} which was in good agreement with the J_{SC} values from J-V measurement.

The parameters of solar cells including PCE, FF, J_{SC} and V_{OC} are quite reproducible. Figure 5(c)-(f) exhibit the histograms of PV parameters. Most PCEs occur between 14% and 18% with the average of ~16%. The fill factor (FF) is mostly in the range of 76 and 78. J_{SC} is mostly in the range from 18 to 21 mA/cm2. V_{OC} is in the range from 1.04 to 1.07V. DMSO solvent vapor annealing indeed improved the performance of perovskite solar cells reproducibly. To the best of our knowledge, for the two-step method, our PCE is the third

highest after Seok et al. [25] and Grazel et al. [6] It should be noted that in our method we did not use $PbBr_2$ and FAI, and if these two components were used, the PCE should be higher than 18.5%.

3. Conclusion

Based on solvent annealing, PbI_2 films were annealed in different solvent atmospheres including DMF, DMSO, Acetone and Isopropanol (IPA). We found that solvent annealing of PbI_2 in the DMF, Acetone, and IPA atmospheres caused dense PbI_2 films, which prevent PbI_2 from complete conversion to $CH_3NH_3PbI_3$. Unlike the above processes, employing the DMSO solvent annealing process for PbI_2 resulted in porous PbI_2, which help complete conversion of PbI_2 to perovskite with larger crystal grains. Solar cells fabricated using the DMSO solvent annealing process exhibit the best efficiency of 18.5% with a fill factor of 76.5%.

4. Experiment Section

Materials. PbI_2, CH_3NH_3I, titanium diisopropoxide bis(acetylacetonate) and spiro-OMeTAD were purchased from Sigma-Aldrich. Titanium dioxide nanoparticles (20nm particle size) and solvents, 2-Propanol (IPA, 99. 5%) and DMF, DMSO, and acetone, were provided by Dyesol and Kelon respectively.

Device Fabrication. FTO glass substrates were cleaned sequentially in alkaline detergent, acetone, ethanol, and DI water for 15 minutes each, followed by drying with N_2 flow. A compact layer of TiO_2 was deposited via spray pyrolysis at 450°C from a precursor solution of titanium diisopropoxide bis (acetylacetonate) in ethanol (volume ratio 1:39). The films were annealed at 500°C for 20 minutes and then cooled down to room temperature. The

mesoporous TiO_2 scaffold was spin-coated at 5000 rpm for 30s and annealed at 500°C for 30 minutes, in which the pristine paste was diluted in ethanol (weight ratio, 2:7). $CH_3NH_3PbI_3$ was synthesized using the two-step spin coating method and the following experiments except for gold deposition were carried out in a glove box in nitrogen. PbI_2 solutions in DMF (1M) were first spin-coated onto the substrates at 3500 rpm and 5000 rpm for 3s and 5s respectively. The films were annealed in nitrogen (called thermal annealing) or in different solvent ambiences (DMF, IPA, DMSO and Acetone) at 45°C for 5 min and then annealed at 100°C in N_2 (thermal annealing) or in different solvent ambiences as above for 5 min. The volume of the solvent dropped on the surface of the hot plate is 60 μl. During the second spin-coating process, 200 μl solution of CH_3NH_3I in isopropanol (8mg/ml) was loaded on PbI_2 films for 45s, which was spun at 4000 rpm for 20s and dried at 100°C in N_2 for 5 min. The substrates were subsequently covered with a 72.3 mg/ml solution of spiro-OMeTAD in 1 ml chlorobenzene with 28.8 μl of added 4-tert-butylpyridine, 17.5 μl of a stock solution of 520 mg ml^{-1} lithium bis(trifluoromethylsulphonyl)imide in acetonitrile and 29 μl of 520 mg ml^{-1} tris (2-(1H-pyrazol-1-yl)-4-tert-butylpyridine) cobalt(Ⅲ) bis (trifluoromethylsulphonyl) imide in acetonitrile. This solution was spin-coated at 4000 rpm for 30s. Finally, 80nm of a gold film was deposited using thermal evaporation.

Measurement and Characterization

X-ray diffraction (XRD) diagrams were carried out using a Bede D1 system with Cu Kα radiation. Scanning electron microscope (SEM) images were obtained using field emission fitting SEM (FEI-Inspect F50, Holland). The UV-vis absorption spectrum were measured by an ultraviolet-visible (UV–vis) spectrophotometer (Schimadzu UV-3101 PC).Current-voltage

measurements were carried out using Keithley 2400 under AM 1.5G illuminations (1000W/m^2) from a solar simulator (Newport Oriel Solar 3A Class AAA, 64023A). The AM 1.5G sun light (100 mW/cm^2) was calibrated using a standard Si-solar cell (Oriel, VLSI standards). EIS measurements were measured with electrochemical workstation (chi660d). The applied voltage perturbation had an AC amplitude of 35 mV with a frequency from 1 MHz to 100 Hz. The impedance parameters were simulated by fitting of impedance spectrum through Z-view software.

Acknowledgement

This work was supported by National Natural Science Foundation of China under Grant Nos.61474016 and 61405026, 61371046, 61421002, 6157031208, 61471085, and National Higher-education Institution General Research and Development Fund (ZYGX2014J044), Projects of International Cooperation of Sichuan Province (No.2014HH0041). This work was also partially supported by University of Kentucky and Advanced Semiconductor Processing Technology, LLC.

Reference

1 A. Kojima, K. Teshima, Y. Shirai and T. Miyasaka, J. Am. Chem. Soc, 2009, **131**, 6050.

2 D. Bi, M. W. Tress, I. Dar, P. Gao, J. Luo, C. Renevier and J. D. Decoppet, Science. Adv, 2016, **2**, 1501170.

3 H. S. Kim, C. R. Lee, J. H. Im, K. B. Lee, T. Moehl, A. Marchioro, M. Grätzel, and N. G. Park, Sci. Rep-UK, 2012, **2,** 591.

4 J. Burschka, N. Pellet, S. J. Moon, R. Humphry-Baker, P. Gao, M. K. Nazeeruddin and M. Grätzel, Nature, 2013, **499**, 316.

5 J. H. Im, I. H. Jang, N. Pellet, M. Grätzel and N. G. Park, Nat. Nanotechnol, 2014, **9**, 927.

6 C. Yi, X. Li, J. Luo, S, M. Zakeeruddin and M. Grätzel, Adv. Mater, 2016, **28**, 2964.

7 J. H. Im, J. Luo, M. Franckevičius, N. Pellet, P. Gao, T. Moehl and N. G. Park, Nano. Lett, 2015, **15**, 2120.

8 Z. Xiao, Q. Dong, C. Bi, Y. Shao, Y. Yuan and J. Huang, Adv. Mater, 2014, **26**, 6503.

9 D. Liu, L. Wu, C. Li, S. Ren, J. Zhang and W. Li, L. Feng, ACS. Appl. Mater. Inter, 2015, **7**, 16330.

10 E. Zheng, X. F. Wang, J. Song, L. Yan, W. Tian and T. Miyasaka, ACS. Appl. Mater. Inter, 2015, **7**, 18156.

11 J. Liu, C. Gao, X. He, Q. Ye, L. Ouyang, D. Zhuang and W. Lau, ACS. Appl. Mater. Inter, 2015, **7**, 24008.

12 H. Yu, X. Liu, Y. Xia, Q. Dong, K. Zhang, Z. Wang and Y. Li, J. Mater. Chem. A, 2016, **4**, 321.

13 C. Liu, K. Wang, C. Yi, X. Shi, A. W. Smith, X. Gong and A. J. Heeger, Adv. Funct. Mater, 2016, **26**, 101.

14 N. J. Jeon, J. H. Noh, Y. C. Kim, W. S. Yang, S. Ryu and S. I. Seok, Nat. Mater, 2014, **13**, 897.

15 N. Ahn, D. Y. Son, I. H. Jang, S, M. Kang, M. Choi and N. G. Park, J. Am. Chem. Soc, 2015, **137**, 8696.

16 H. S. Ko, J. W. Lee and N. G. Park, J. Mater. Chem. A, 2015, **3**, 8808.

17 Y. Wu, A. Islam, X. Yang, C. Qin, J. Liu, K. Zhang and L. Han, Energ. Environ. Sci,

2014, **7**, 2934.

18 H. Zheng, W. Wang, S. Yang, Y. Liu and J. Sun, RSC. Adv, 2016, **6**, 1611.

19 A. Dualeh, N. Tétreault, T. Moehl, P. Gao, M. K. Nazeeruddin and M. Grätzel, Adv. Funct. Mater, 2014, **24**, 3250.

20 T. Zhang, M. Yang, Y. Zhao and K. Zhu, Nano. Lett, 2015, **15**, 3959.

21 A. Wakamiya, M. Endo, T. Sasamori, N. Tokitoh, Y. Ogomi, S. Hayase and Y. Murata, Chem. Lett, 2014, **43**, 711.

22 V. Gonzalez-Pedro, E. J. Juarez-Perez, W, S. Arsyad, E. M. Barea, F. Fabregat-Santiago, I. Mora-Sero and J. Bisquert, Nano. Lett, 2014, **14**, 888.

23 D. S. Lee, W. Kim, B. G. Cha, J. Kwon, S. J. Kim, M. Kim and J. H. Park, ACS. Appl. Mater. Inter, 2015, **8**, 449.

24 M. I. Dar, M. Abdi-Jalebi, N. Arora, M. Grätzel and M. K. Nazeeruddin, Adv. Energy. Mater, 2016, **6**, 1501358

25 W. S. Yang, J. H. Noh, N. J. Jeon, Y. C. Kim, S. Ryu, J. Seo and S. I. Seok, Science, 2015, **348**, 1234.

26 J. W. Lee, D. J. Seol, A. N. Cho and N. G. Park, Adv. Mater, 26, **29**, 4991.

27 H. Li, S. Li, Y. Wang, H. Sarvari, P. Zhang, M. Wang and Z. Chen, Sol. Energy, 2016, **126**, 243.

28 M. Wang, S. Li, P. Zhang, Y. Wang, H. Li and Z. Chen, 2015, Chem. Phys. Lett, HYS LETT, **639**, 283.

29 H. S. Kim and N. G. Park, 2014,J. Phys. Chem. Lett, 5, **17**, 2927.

Figure1: (a) The schematic diagram of annealing methods for PbI_2 films; (b) UV-vis absorption spectra of PbI_2 and (c) $CH_3NH_3PbI_3$ using different annealing methods of TA-TA, DMF SA-TA, DMF SA-SA, and DMF TA-SA; (d) XRD patterns of PbI_2 fabricated by DMF SA-TA and TA-TA method; (e) forward and reverse scan J-V curves of perovskite solar cells using different annealing methods.

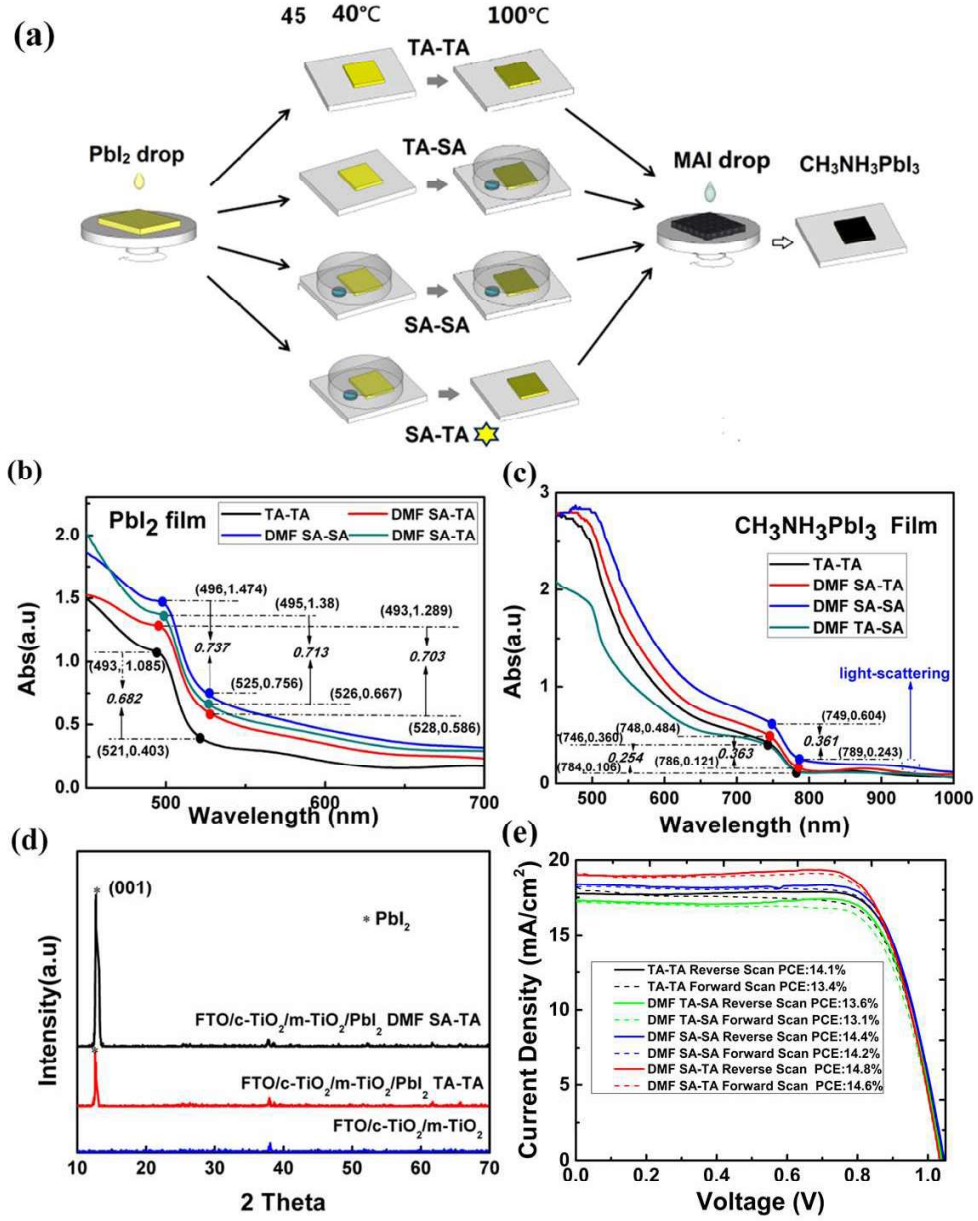

Figure2: (a)-(e) SEM top views of PbI_2 films treated by TA-TA, DMF SA-TA, DMSO SA-TA, Acetone SA-TA and IPA SA-TA process; (f)-(j) Surface SEM images of $CH_3NH_3PbI_3$ via TA-TA, DMF SA-TA, DMSO SA-TA, Acetone SA-TA and IPA SA-TA processes.

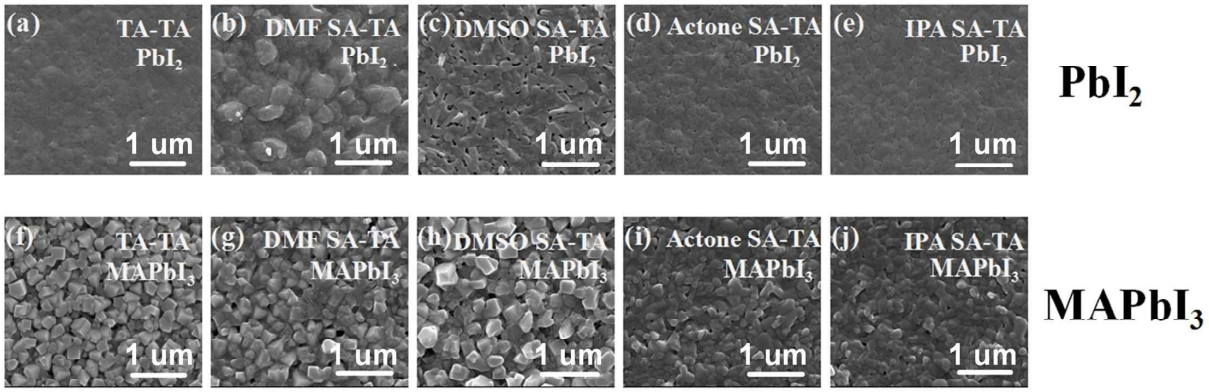

Figure3: (a)-(b) XRD patterns and UV-vis absorption spectra of PbI_2 films treated by TA-TA, DMF SA-TA, DMSO SA-TA, acetone SA-TA, and IPA SA-TA processes; (c) The photos of PbI_2 and $CH_3NH_3PbI_3$ films under different atmosphere. (d)-(e) UV-vis absorption spectra and XRD patterns of $CH_3NH_3PbI_3$ via TA-TA, DMF SA-TA, DMSO SA-TA, acetone SA-TA and IPA SA-TA processes; (f) J-V curves of the solar cell samples with TA-TA, DMF SA-TA, DMSO SA-TA, acetone SA-TA and IPA SA-TA processes.

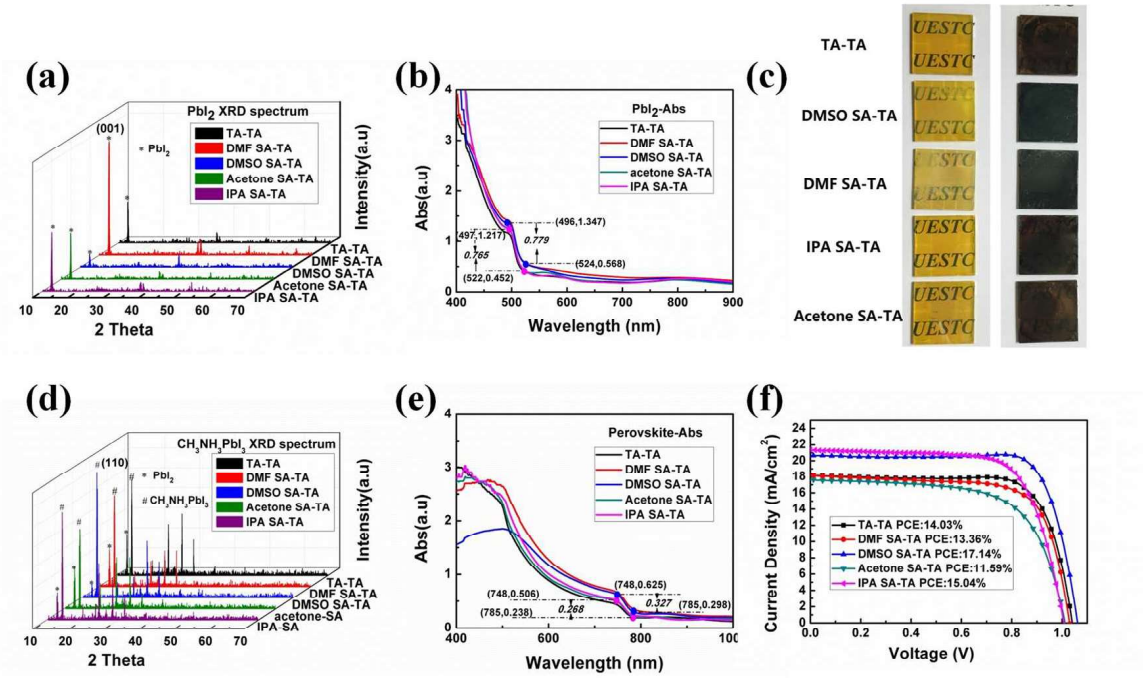

Figure4: (a) The schematic diagram of solvent annealing mechanism; SEM cross-section image of $CH_3NH_3PbI_3$ with thermal annealing (TA-TA) (b) and DMSO solvent annealing (DMSO SA-TA) (c); (d) The EIS Nyquist profiles of perovskite films fabricated by TA-TA and DMSO SA-TA processes.

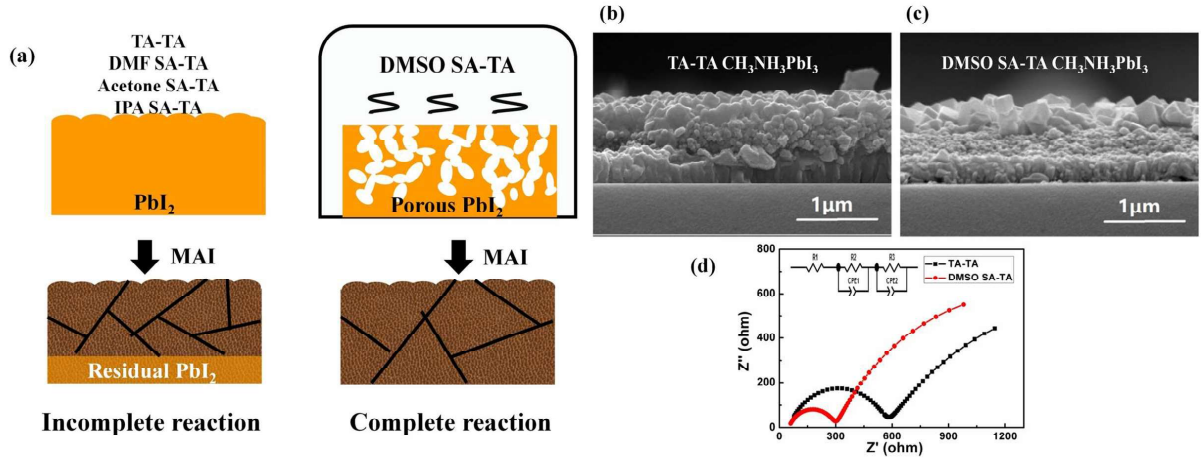

Figure.5 (a)-(b) J-V curves (forward and reverse scan) and EQE of the best performance device obtained from DMSO SA-TA solvent annealing process; (c) Distribution of the efficiency, V_{OC}, FF and J_{SC} of the devices with DMSO SA-TA process.

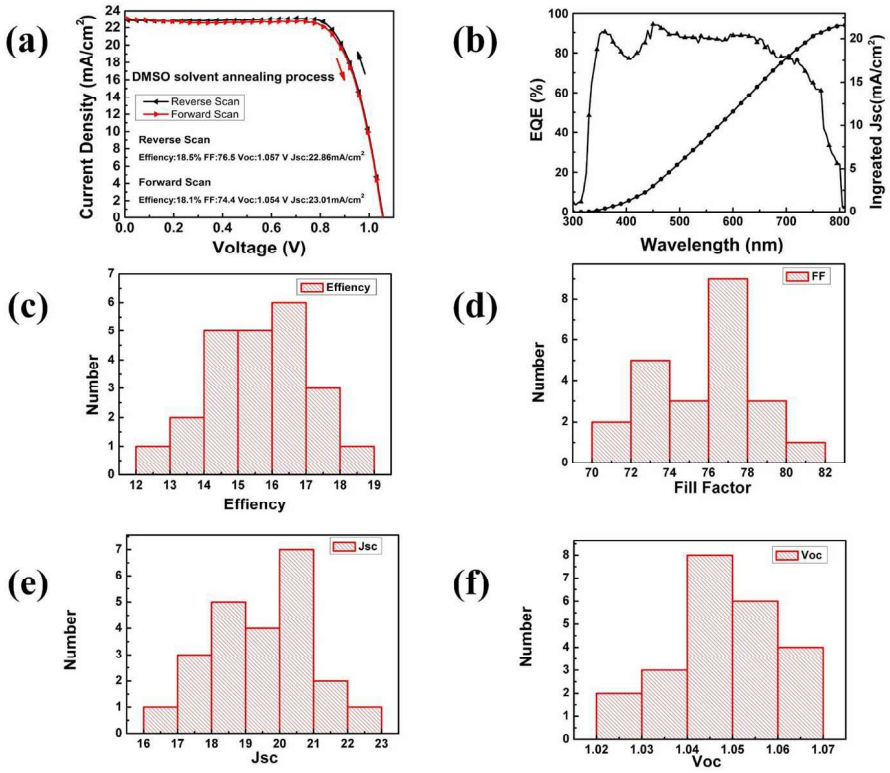

Table1: Performance (V_{OC}, J_{SC}, FF and PCE) of devices using TA-TA, DMF SA-TA, DMSO SA-TA, acetone SA-TA and IPA SA-TA processes.

Employing different solvent annealing processes	V_{oc} (V)	J_{sc} (mA/cm^2)	FF (%)	PCE (%)
TA-TA	1.04	18.12	74.3	14.0
DMF SA-TA	1.03	18.11	71.7	13.4
DMSO SA-TA	1.06	20.68	78.1	17.1
Acetone SA-TA	1.01	17.59	65.1	11.6
IPA SA-TA	1.02	21.54	68.3	15.0

Supplement Information

Solvent Annealing of PbI_2 for High-Quality Crystallization of Perovskite Films for Solar Cells with Efficiency Exceeding 18%

Yafei Wang[a], Shibin Li[a*], Peng Zhang[a], Detao Liu[a], Xiangling Gu[a], Hojjatollah Sarvari[b], Zhongbiao Ye[a,b], Jiang Wu[c], Zhiming Wang[d], and Zhi David Chen[a,b*]

[a] State Key Laboratory of Electronic Thin Films and Integrated Devices, and School of Optoelectronic Information, University of Electronic Science and Technology of China (UESTC), Chengdu, Sichuan 610054, China

[b] Department of Electrical & Computer Engineering, and Center for Nanoscale Science & Engineering, University of Kentucky, Lexington, Kentucky 40506, USA

[c] Department of Electronic and Electrical Engineering, University College London, Torrington Place, London WC1E 7JE,United Kingdom

[d] Institute of Fundamental and Frontier Sciences, University of Electronic Science and Technology of China, Chengdu, 610054, China

*Corresponding authors: shibinli@uestc.edu.cn, zhichen@engr.uky.edu

In this investigation, using the DMSO SA-TA process, a series of experiment parameters were studied to optimize the performance of solar cells. At first, we studied the TA-TA, DMSO SA-TA, DMSO SA-SA as shown in Figure S1, because the TA-SA process did not result in good results as described in the text. We found that the DMSO SA-TA annealing process is the best among TA-TA and DMSO SA-SA processes. This result is consistent with our previous conclusion using DMF in the text. It should be noted that we used the same petri dish. We studied the effect of different DMSO volumes on the device performance as shown in Figure S2. We found negligible difference in PCE by using different volumes of DMSO solution. We chose the volume of 50 μl in our subsequent experiments. The diameter of m-TiO_2 and the

spin speed of PbI_2 were also investigated (Figure S3 and Figure S4). It can be seen in Figure S3 that m-TiO2 with the diameter of 30 nm results in better PCE. The first spin speed of PbI_2 significantly affected the device performance. As shown in Figure S4, the first spin speeds of 2500 rpm, 3000 rpm, and 3500 rpm resulted in PCEs of 14%, 15.7%, AND 17.1% separately. In addition, we studied thermal annealing (TA) of PbI_2 and the DMSO annealing of PbI_2 at 100°C for 10 min. After thermal annealing at 100°C, PbI_2 exhibits smooth and dense surface, while after annealing PbI_2 in DMSO at 100°C we obtained a surface that looks like needles but are actual many PbI_2 nanowires as shown in Figure S5. This suggests that lower temperature DMSO annealing is better for porous PbI_2.

Figure.S1 J-V curves and device performance of devices fabricated using different annealing processes (TA-TA, DMSO SA-TA and DMSO SA-SA).

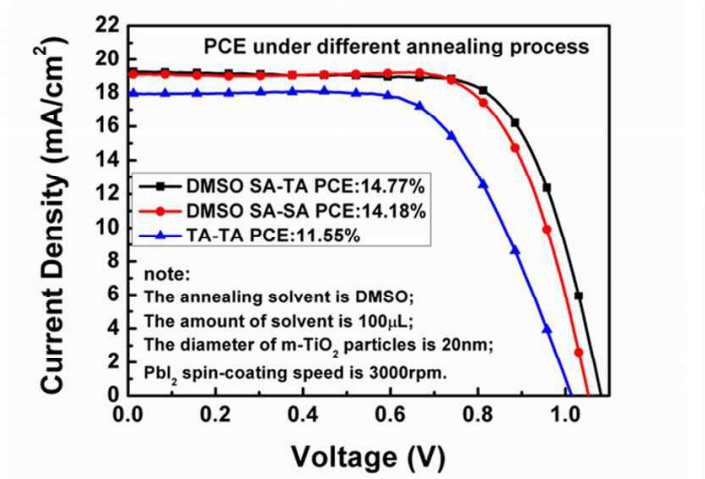

Annealing method	V_{oc} (V)	J_{sc} (mA/cm^2)	FF (%)	PCE (%)
DMSO SA-TA	1.08	19.27	70.9	14.8
DMSO SA-SA	1.05	19.11	70.5	14.2
TA-TA	1.01	17.94	63.5	11.6

Figure.S2 J-V curves and device performance of solar cells fabricated using different volumes of DMSO solvent in the DMSO SA-TA process.

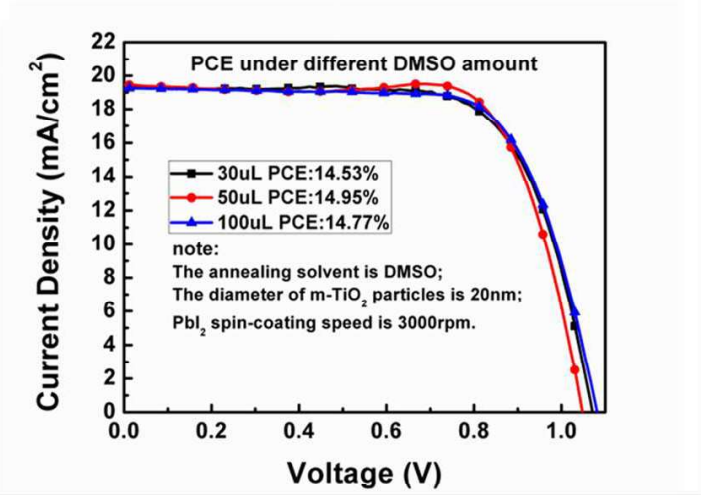

Amount of DMSO in SA process (uL)	V_{oc} (V)	J_{sc} (mA/cm^2)	FF (%)	PCE (%)
30	1.07	19.28	70.4	14.5
50	1.05	19.46	73.4	14.9
100	1.03	20.10	67.5	14.0

Figure.S3 J-V curves and device performance of devices fabricated using m-TiO_2 with different diameters.

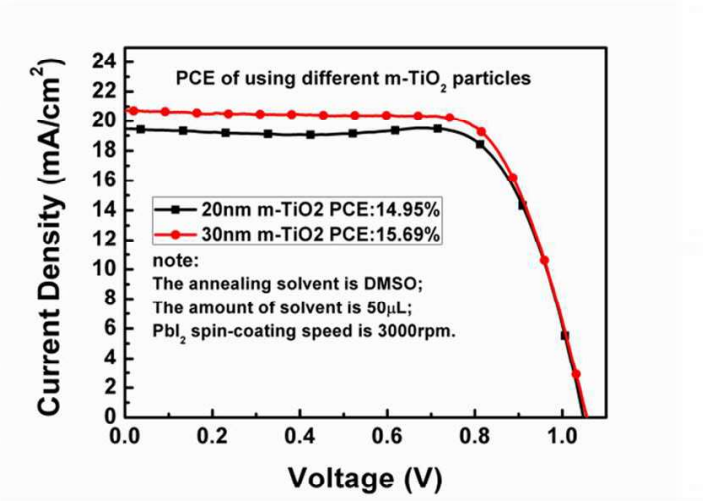

Diameter of m-TiO_2 particles (nm)	V_{oc} (V)	J_{sc} (mA/cm^2)	FF (%)	PCE (%)
20	1.05	19.46	73.4	14.9
30	1.05	20.72	71.7	15.7

Figure.S4 J-V curves and device performance of devices fabricated using different spin-coating speeds for PbI_2.

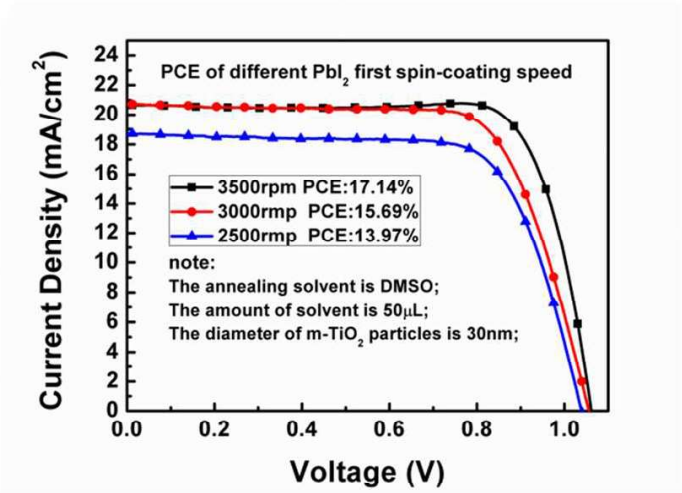

Different spin-coating speed of PbI_2 (rpm)	V_{oc} (V)	J_{sc} (mA/cm^2)	FF (%)	PCE (%)
2500	1.04	18.70	71.9	13.9
3000	1.05	20.72	71.7	15.7
3500	1.06	20.68	78.1	17.1

Figure.S5 SEM images of Surface morphology of PbI_2 films obtained using different annealing processes at 100 °C.

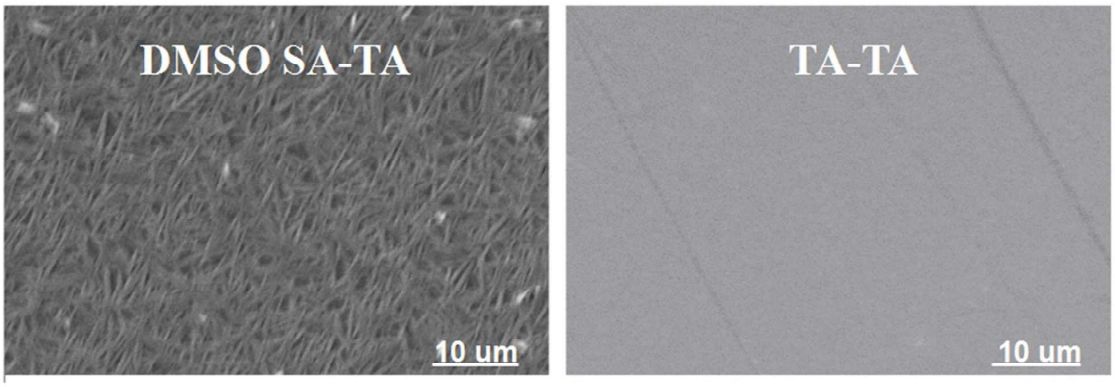

Porous PbI_2 induced by the DMSO solvent annealing leads to large grains of perovskite without residual PbI_2.